S. XIONG [1,2,3,4*]

PROGRESS AND CHALLENGES IN MICROSTRUCTURE AND PROPERTIES OF BORATE MINERAL CHAMBERSITE NANO-$Mn_3B_7O_{13}Cl$: A REVIEW

Borate mineral chambersite ($Mn_3B_7O_{13}Cl$) is a kind of manganese-chloride-borate mineral with great application prospect. China is the only country has the borate mineral chambersite deposits in the world at present. It is of great theoretical and practical significance to develop and utilize raw $Mn_3B_7O_{13}Cl$ and synthetic nano- $Mn_3B_7O_{13}Cl$, and study its microstructure and properties. This review provides an overview of the microstructure, photoluminescence, gamma ray irradiation and neutron irradiation properties, electromagnetic properties, anti-tumor, anti-bacterial properties, as well as friction and wear properties of $Mn_3B_7O_{13}Cl$, which provides a theoretical basis for further development and application of $Mn_3B_7O_{13}Cl$.

Keywords: Borate Mineral Chambersite; $Mn_3B_7O_{13}Cl$; Microstructure; Photoluminescence; Electromagnetic Properties; Friction and Wear

1. Introduction

An uncommon borate mineral called manganboracite has a complex chemical structure called chambersite [1-6]. Manganboracite was initially found in brine extracted from American oil fields in 1957 [7,8]. Following preliminary investigations into its structure and physicochemical characteristics, it was given the name Chambersite ($Mn_3B_7O_{13}Cl$) in 1962, honoring its place of origin [9-12]. Later, this type of mineral was discovered in Mexico, Louisiana, and other locations, but no significant deposit was located [13-15]. The only manganboracite deposit in the world was found in Jixian County, Tianjin, China, up to the early 1970s [16,17]. In the deep ultraviolet range, $Mg_3B_7O_{13}Cl$ and $Zn_3B_7O_{13}Cl$ have most recently been described as new quasi-phase matching crystals [1-3]. TABLE 1 compares these crystal structures with $Mn_3B_7O_{13}Cl$. Due to its diverse structure type and exceptional physicochemical qualities, $Mn_3B_7O_{13}Cl$ has been employed extensively as a borate compound in laser materials, luminous matrix materials, and nuclear protection materials [18,19]. In this paper, the research progress of the microstructure, photoluminescence, gamma ray irradiation, neutron irradiation properties electromagnetic properties, anti-tumor, anti-bacterial properties, and tribologi-

cal properties of $Mn_3B_7O_{13}Cl$ are summarized, which provides a theoretical basis for the further development and application of $Mn_3B_7O_{13}Cl$.

TABLE 1

Crystal Data of $Zn_3B_7O_{13}Cl$, $Mg_3B_7O_{13}Cl$ and $Mn_3B_7O_{13}Cl$

Empirical formula	$Zn_3B_7O_{13}Cl$ [1,2]	$Mg_3B_7O_{13}Cl$ [3]	$Mn_3B_7O_{13}Cl$ [4]
Unit cell dimensions	a = 8.5345Å b = 8.5345 Å c = 20.9545 Å	a = 8.6559 Å b = 8.6320 Å c = 12.2108 Å	a = 8.68 Å b = 8.68 Å c = 12.26 Å
Crystal system Space	Monoclinic R3c	Orthorhombic Pca21	Orthorhombic Pca21 (29)
Band gaps (eV)	6.53	5.56	5.65

2. Microstructure, properties, and synthesis of $Mn_3B_7O_{13}Cl$

By using the nuclear γ-ray resonance method in 1975, the former Soviet Union academician Belov et al. [4] discovered that the chambersite mineral's fundamental structure is a boron-oxygen skeleton structure. Its chemical formula is $Mn_3B_7O_{13}Cl$,

[1] NANJING INSTITUTE OF TECHNOLOGY, COLLEGE OF MATERIALS ENGINEERING, NANJING JIANG SU 211167, PR CHINA
[2] JIANGSU KEY LABORATORY OF ADVANCED STRUCTURAL MATERIALS AND APPLICATION TECHNOLOGY, NANJING JIANG SU 211167, P.R CHINA
[3] JINLING INSTITUTE OF TECHNOLOGY, COLLEGE OF MATERIALS ENGINEERING, NANJING JIANG SU 211167, P.R CHINA
[4] UNIVERSITY OF SCIENCE AND TECHNOLOGY BEIJING, SCHOOL OF MATERIALS SCIENCE AND ENGINEERING, BEIJING 100083, CHINA

* Corresponding author: jxbjxs2008@163.com

and its crystal structure is the regular square system. Chambersite has a high protrusion, an evident rough surface, no cleavage, crack development, and interference colors that range from first order gray white to yellow. It is granular, colorless, and transparent. Further research on the physicochemical characteristics of chambersite was conducted by Xiao et al. [5]. Chambersite often has an uneven granular shape, an oolite aggregate with bean-like crystals, and an oil-glass sheen. Chambersite has a seashell-uneven fracture but no cleavage or crack growth. It is white or off-white in color, has a Mohs hardness of 7, and has a density of (3.48 ± 0.01) g/cm^3. Raw chambersite minerals underwent differential thermal analysis (DTA), and the outcomes are depicted in Fig. 1. The differential thermal curve of chambersite, as can be seen, consists of two endothermic troughs. Among them, the peak valley of endothermic reactions at around 400°C is connected to the transition of the mineral phase from the low temperature rhombic system to the high temperature equiaxial system, and the peak valley at around 1070°C is brought on by the melting of the mineral.
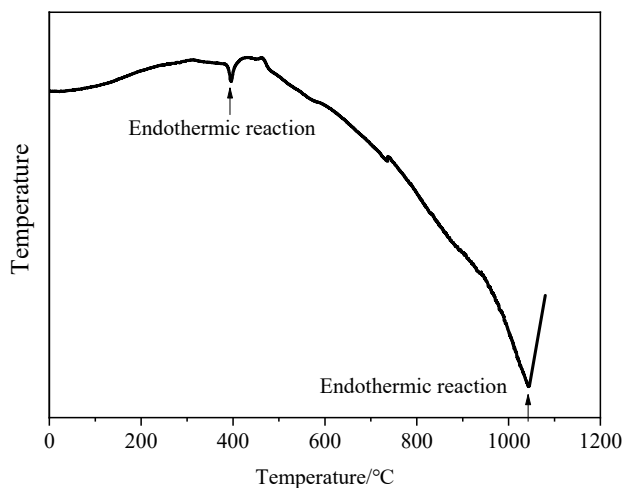

Fig. 1. Differential thermal analysis curve of chambersite

Centimeter-sized chambersite ($Mn_3B_7O_{13}Cl$) crystals were formed using a melt growth technique, according to Jiesen et al. [6]. At ambient temperature, $Mn_3B_7O_{13}Cl$ crystallizes as the polar space group Pca21. The study of synthetic manganite has advanced significantly since the discovery of manganite in Jixian, China. In 1983, Zeng Yishan from the Department of Geology of Peking University synthesized $Mn_3B_7O_{13}Cl$ at 100°C and 200°C by hydrothermal synthesis using $MnCl_2$-$NaB(OH)_4$-H_2O system, $Na_2B_4O_7 \cdot 10\ H_2O + Mn\ Cl_2 \cdot 4\ H_2O + H_2O$ [7]. In recent years, Cao et al. [8] reported that the synthesized nano-sized $Mn_3B_7O_{13}Cl$ has the same crystal structure as raw $Mn_3B_7O_{13}Cl$ by $MnCl_2$ and $Na_2B_4O_7$ as raw materials using sol-gel method, $12\ MnCl_2 + 7\ Na_2B_4O_7 + 3\ H_2O = 4\ Mn_3 B_7O_{13}Cl + 14\ NaCl + 6\ HCl$. An X-ray diffraction (XRD) profile of a nano- $Mn_3B_7O_{13}Cl$ crystal is shown in Fig. 2. The findings demonstrate that both synthetic and natural $Mn_3B_7O_{13}Cl$'s major diffraction peak position and relative strength are matched to that of the peak on the standard powder diffraction file (PDF). The

crystal structure of $Mn_3B_7O_{13}Cl$ belongs to the orthorhombic system, with the spatial point group Pca21 (29). The parameters of the cell are as follows: $a = 0.868$ nm, $b = 0.868$ nm, $c = 1.226$ nm, $\alpha = \beta = \gamma = 90°$. A three-dimensional (3D) borate framework can be seen in $Mn_3B_7O_{13}Cl$ is made up of the functional building blocks B_1O_4–B_6O_4 (six BO_4 units) and B_7O_3 (one B_7O_3 unit), which are shown in Fig. 2(a). A three-dimensional B-O network is created by connecting four B_7O_{13} units with various stereo-isomeric configurations further using bridging oxygen atoms [Fig. 2(b)]. A complex 3D network [Fig. 2(d)] is created by the intertwining of the B_7O_{13} groups and $ClMn_6$ octahedron [Fig. 2(c)]. According to the Scherer formula, the grain sizes of the synthesized $Mn_3B_7O_{13}Cl$ and raw $Mn_3B_7O_{13}Cl$ are 48.4 nm and 68.4 nm by Scherer formula. By using scanning electron microscopy (SEM) and transmission electron microscopy (TEM), the microscopic morphology of natural $Mn_3B_7O_{13}Cl$ and nano-sized synthetic $Mn_3B_7O_{13}Cl$ was observed and given in Fig. 3. The $Mn_3B_7O_{13}Cl$ particles are discovered to be spheroidal and uniformly dispersed, with an average particle size of about 50 nm, which is consistent with the outcomes predicted by the Scherer formula.
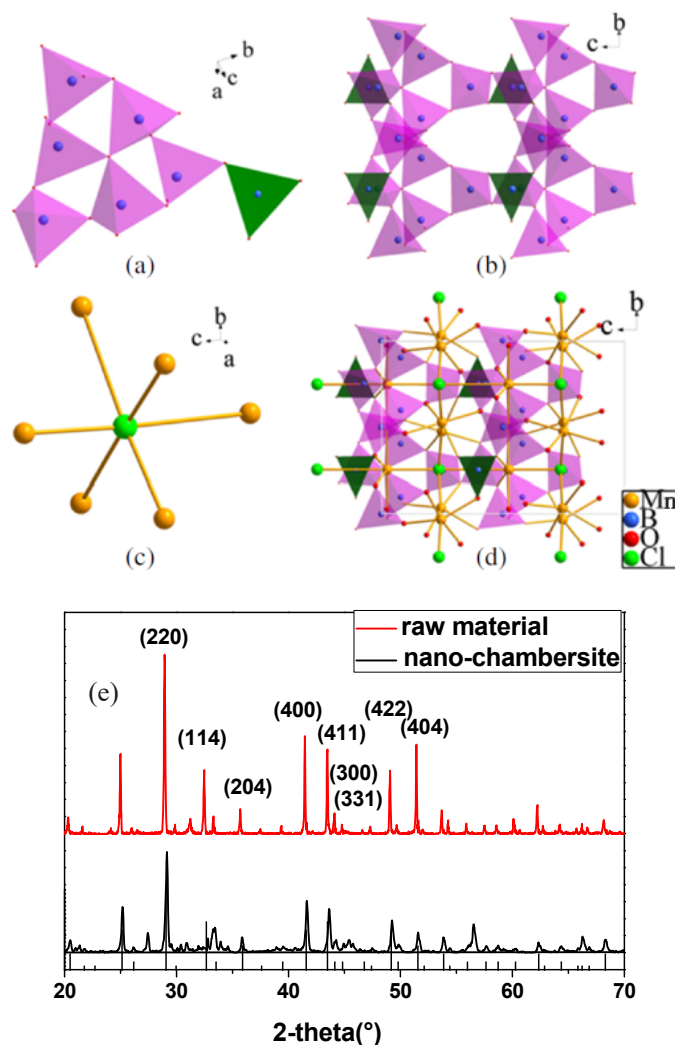

Fig. 2. Crystal structure of $Mn_3B_7O_{13}Cl$: (a) B_7O_{13} group, (b) four B_7O_{13} groups, (c) $ClMg_6$ octahedron, (d) crystal structure of $Mn_3B_7O_{13}Cl$. and (e) XRD patterns of nano-synthesized and raw $Mn_3B_7O_{13}Cl$
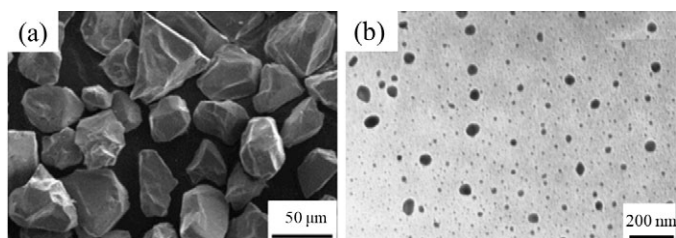
Fig. 3. SEM images of raw $Mn_3B_7O_{13}Cl$ (a) and TEM morphology of synthesized $Mn_3B_7O_{13}Cl$ (b)

Fig. 4. HREM images (a), calculated images (b) and diffraction patterns (c) of synthetic $Mn_3B_7O_{13}Cl$

Further research was done on the high-resolution phase, computational phase, and diffraction spectrum produced by the Fourier transform of the synthetic $Mn_3B_7O_{13}Cl$ [8], and the outcomes are shown in Fig. 4. The plane spacing d of the produced $Mn_3B_7O_{13}Cl$ crystal (111) is 0.572 nm, which is 4.6% larger than that of the standard image library. Numerous atomic point defects can be seen in Fig. 4(a), which results in the lattice distortion depicted in point A. The high-resolution phase, computational phase and the diffraction spectrum obtained by Fourier transform of the synthetic $Mn_3B_7O_{13}Cl$ were further studied [8], and the results are given in Fig. 4. The synthesized $Mn_3B_7O_{13}Cl$ crystal grows completely, and the plane spacing d of (111) crystal is 0.572 nm, which increases by 4.6% compared with the standard image library. In Fig. 4(a), there are many atomic point defects, which cause certain lattice distortion, as shown in point A. It can be determined that the corresponding position at point A is the location of the point defect created by the separation of the boron atom from its equilibrium position through the simulation phase and skeleton diagram calibration of the atomic phase. The B-O bond is lengthened by the macromolecular structure of $Mn_3B_7O_{13}Cl$, which lowers the energy barrier for boron atoms to leave their initial equilibrium position, allowing them to break free and produce point defects. Since B^{3+} has a smaller atomic radius than Mn^{2+}, which is consistent with the lattice distortion in Fig. 4. Using computer simulation, the predicted phase, simulation diagram, and molecular skeleton diagram of synthetic $Mn_3B_7O_{13}Cl$ were displayed in Fig. 5.

3. Photoluminescence properties of $Mn_3B_7O_{13}Cl$

Borate luminescent materials activated by transition ions are an important component system of luminescent materials, whose composition and structure are relatively complex. Mn element is an important activator in solid luminescent materials. For $Mn_3B_7O_{13}Cl$, the Mn element is a transition metal ion with $4s^2 3d^5$ electron configuration, and has an incomplete filled d-shell electrons. In $4s^2$ electron shell, the electron configuration is the same as that of Ar electron structure. When the Mn element is ionized, it always loses two 4s electrons first, leaving only the d-shell electrons. Based on the examination of its microstructure, Xiong et al. [8] investigated $Mn_3B_7O_{13}Cl$'s luminescence characteristics in more detail. As shown in Fig. 6, emission spectra of the synthetic $Mn_3B_7O_{13}Cl$ were obtained at wavelengths of
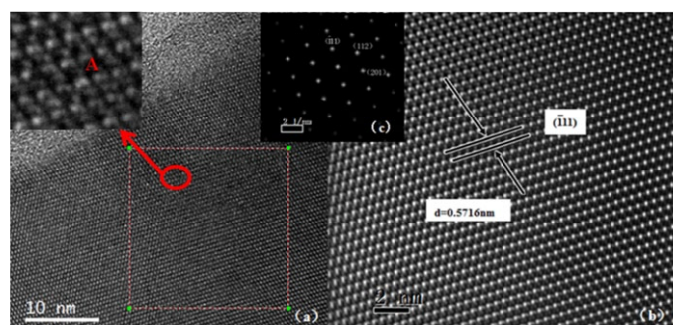

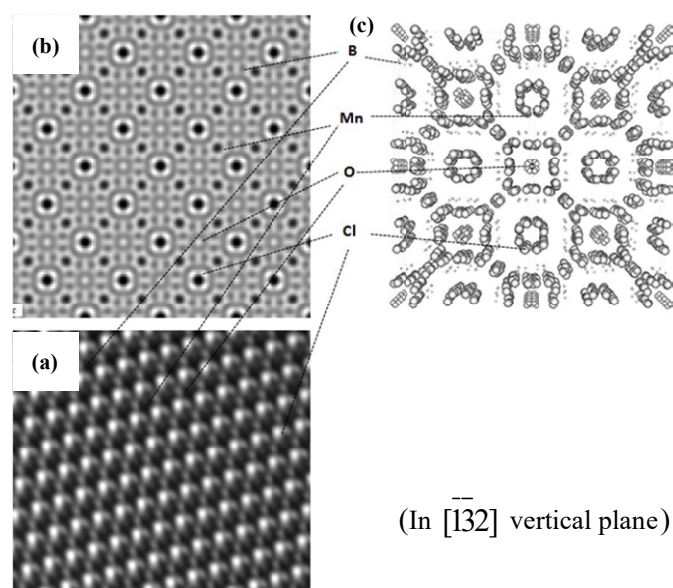(In $[\overline{1}\overline{3}2]$ vertical plane)

Fig. 5. Calculated images (a), simulated images (b) and molecular skeleton diagram (c)of synthetic $Mn_3B_7O_{13}Cl$

450, 460, 470, 480, and 490 nm (a). The emission spectra of $Mn_3B_7O_{13}Cl$ shows two emission peaks, one in the green band (500-540 nm) and the other in the red band (670-730 nm), as can be seen in Fig. 6.

It is simple to assume that the luminescence of $Mn_3B_7O_{13}Cl$ is the luminescence of the Mn element. The transfer of Mn^{2+} from $^4T_1(G)$ to $^6A_1$ (S) causes luminescence [9-12], and the ligand field has a greater impact on the energy level of $^4T_1(G))$ than $^6A_1$ (G) and $^4E(G)$. The green luminescence of the Mn^{2+} ion embedded in the tetrahedron, which shows a transition from $^4T_1(G)$ to $^6A_1$ (S) under the excitation of short wavelength, is therefore facilitated by the point defect of B^{3+} ion observed in the crystal in Fig. 6. Nevertheless, the majority of Mn^{2+} ions emit red light due to their position located in the middle of the octahedral coordination and have a greater ligand field than the tetrahedral coordination. Additionally, the emission spectrum is redshifted as the excitation wavelength increases. When the excitation wavelength is increased by 10 nm, the average rise in the green wavelength is 10 nm, matching the increase in the excitation wavelength, while the average increase in the red wavelength is 15 nm, matching the increase in the excitation wavelength. Only
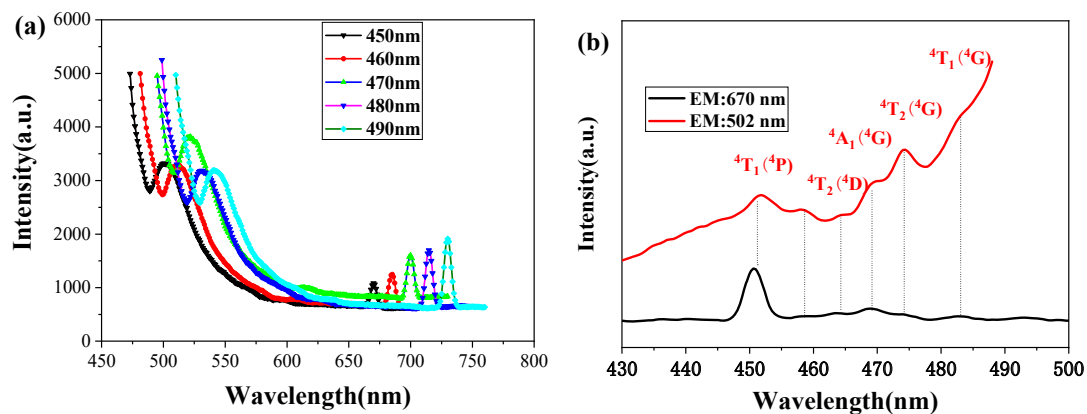
Fig. 6. Emission spectra (a) and excitation spectra (b) of Mn^{2+} in synthetic $Mn_3B_7O_{13}Cl$ at different excitation wavelengths

silver nanoclusters have this behavior of shifting with excitation wavelength been documented in crystalline materials [13-16]. $Mn_3B_7O_{13}Cl$ nanoparticles are clustered, which causes the intensity of the crystal field in Mn^{2+} to fluctuate depending on the degree of agglomeration. $Mn_3B_7O_{13}Cl$'s emission spectrum is thus redshifted. Fig. 6(b) shows the excitation spectra measured at 502 nm (green light) and 670 nm (red light). These excitation peaks can be identified from the excitation spectra as transitions from the ground state $^6A_1$ to the excited state $^4T_2(^4G)$, $^4A_1/^4E(^4G)$, $^4T_2(^4D)$, $^4T_1(^4P)/^4E(^4D)$, respectively. These ground-state $^6A_1$ excitations are slower than those from $^4T_1$. As a result, the transition from the d-d conversion of Mn^{2+} to $^4T_1$-$^6A_1$ is represented by the luminescence of $Mn_3B_7O_{13}Cl$.

4. Gamma ray irradiation and neutron irradiation properties of $Mn_3B_7O_{13}Cl$

In 2003, Sayed et al. [20] studied and explored the shielding properties of ilmenite/epoxy resin composites for neutron and γ rays. In 2004, Kamoshida et al. [21] developed an epoxy-based radiation shielding material that can be used in storage containers of spent nuclear fuel, with a temperature of 150℃~200℃. In 2007, Morioka et al. [22] developed boron containing resin resistant to 300℃ and applied it in JT-60 nuclear fusion device. In the field of radiation protection, the development of shielding materials is a very important link, whose performance directly determines the health of personnel in nuclear facilities. Therefore, how to reduce the radiation dose in the working area to a greater extent and how to effectively attenuate the energy of rays have become the main objectives of the development of shielding materials [23,24]. The changes of the luminescence properties of $Mn_3B_7O_{13}Cl$ under gamma rays lay a certain research foundation for its application as nuclear detection materials. TEM images of raw $Mn_3B_7O_{13}Cl$ after cobalt-60 gamma ray irradiation are shown in Fig. 7. There are many bubblelike dislocation rings (position A) and line defects caused by dislocation accumulation (position B) in the $Mn_3B_7O_{13}Cl$ crystal, which were not found in the electron microscope observation before irradiation [25,26].
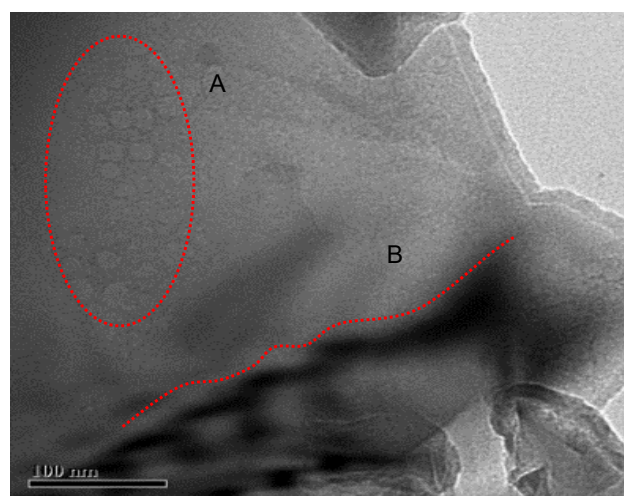

Fig. 7. TEM image of raw $Mn_3B_7O_{13}Cl$ after Cobalt-60 gamma-ray irradiation

The basic structure of chambersite is a boron-oxygen skeleton [27-33]. The melting point is 1065℃, and the hardness is 7 [34]. Lots of scholars studied the mineral processing test, which shows that the product grade, undressed ore recovery rate, and production efficiency of manganese ore concentrate can be up to 29×10^{-2}, 70%, and 33%, respectively. And the B_2O_3 mineral grade and recovery rate can reach 10×10^{-2} and 80% [15]. Chambersite was also found to have electromagnetic [35], friction, and wear resistance [36-38]. It is well known that element B has excellent absorption capacity for thermal neutrons. Furthermore, in previous studies, Mn and Fe or their compounds were used as -ray shielding additives [39,40]. In addition, the study on the microstructure, luminescence, and medical properties of nano-$Mn_3B_7O_{13}Cl$ by gamma ray radiation indicates that the chamber materials have important application value in the field of shielding materials [41]. Fig. 8 displays the gamma-ray-induced emission spectra of synthesized -$Mn_3B_7O_{13}Cl$ at 480 and 490 nm. The findings demonstrate that gamma radiation increases the luminescence intensity of raw -$Mn_3B_7O_{13}Cl$ in the red band by 3.5 times while increasing the luminescence intensity of synthesized nano-$Mn_3B_7O_{13}Cl$ by 3 times. The two samples' emission spectra had identical peak positions. Normal conditions will
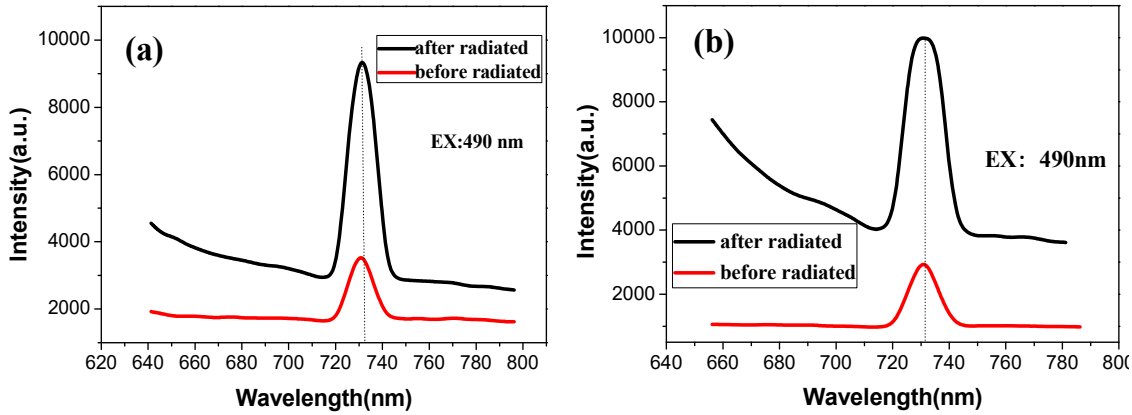
Fig. 8. Emission spectra of synthetic (a) and raw (b) $Mn_3B_7O_{13}Cl$ after irradiated by Gamma-ray excited at 490 nm wavelength

result in an electron trap formed by microscopic structure flaws, which will interfere with the energy level transition of luminous materials and lessen their luminescence intensity. However, as $Mn_3B_7O_{13}Cl$ is exposed to radiation, the strength of the radiation increases. The parity conservation law forbids some transitions because they add anti-parity as a result of structural modifications, which would negate the conservation law and allow for the initial prohibited transition. As a result, the sample exposed to gamma rays has a higher radiation intensity than the unirradiated sample. This property of the irradiation-induced intensity shift makes $Mn_3B_7O_{13}Cl$ a suitable gamma ray detector.

In the composite coating, epoxy resin contains many hydrogen and carbon elements, which have a large neutron scattering cross section and can effectively change high energy fast neutrons into low energy slow neutrons through scattering effect, which is more conducive to the absorption of neutrons by the material [42,43]. Boron is an essential component of neutron shielding materials and has a significant role in neutron capture in $Mn_3B_7O_{13}Cl$ [44]. In the Fukushima nuclear power plant accident, boric acid was sprayed on the accident site. Boric acid and borax are both common neutrons shielding materials. $Mn_3B_7O_{13}Cl$ has a boron content that is 2.78 times higher than that of borax and 2.17 times higher than that of boric acid at the same volume. $Mn_3B_7O_{13}Cl$ can therefore be applied

in a significant way to the field of neutron shielding materials [45]. The luminescence intensity of the epoxy resin/ball-milling $Mn_3B_7O_{13}Cl$ coating is raised by 147% following exposure to 470 nm excitation light, as shown in Fig. 9. The intensity of the natural $Mn_3B_7O_{13}Cl$ composite coating changes more than that of the artificial nano-$Mn_3B_7O_{13}Cl$ composite coating, and the spectrum variation after neutron irradiation is similar to that after gamma ray irradiation. This is also due to the fact, that under the influence of such high-energy neutrons, some transitions that are prohibited by the parity conservation law add anti-parity when the structure changes, which destroys conservation and makes the transition that was previously prohibited possible, increasing the luminescence intensity.

5. Electromagnetic properties of $Mn_3B_7O_{13}Cl$

$Mn_3B_7O_{13}Cl$ is a polar material with multiple functions [46-52]. $Mn_3B_7O_{13}Cl$ is a rare natural mineral was first found in Chambers County, Texas [53]. In 1964, H. Schmid synthesized millimeter-sized crystals by the CVT process [54]. $Mn_3B_7O_{13}Cl$ is polar and crystallizes in the orthogonal space group Pca21 at room temperature [55]. The distorted polyhedron (ClMn6) generates an intrinsic electric dipole moment and generates thermoelectricity in the system [56]. H. Schmid et al. [57] studied the magnetic behavior of $Mn_3B_7O_{13}Cl$, and the results showed that $Mn_3B_7O_{13}Cl$ is antiferromagnetic, with a TN of about 10k, which was confirmed by neutron diffraction and symmetry analysis. Furthermore, manganese borate nanorods as anodes for lithium-ion batteries were investigated [58]. Borates are the most promising deep ultraviolet NLO materials [59]. Recently, $Mg_3B_7O_{13}Cl$ and $Zn_3B_7O_{13}Cl$ have been reported as new quasi-matching crystals in the deep ultraviolet region [60-62]. $Mn_3B_7O_{13}Cl$ is similar in structure to $Mg_3B_7O_{13}Cl$ and $Zn_3B_7O_{13}Cl$, so its optical properties are also worth studying. Until now, the source of $Mn_3B_7O_{13}Cl$ crystals has been natural minerals or crystals grown by the CVT method [63]. Heterogeneous natural crystals are difficult to be separated, and there are many defects due to insufficient crystal size, which seriously affect further research and application [64,65]. The structural
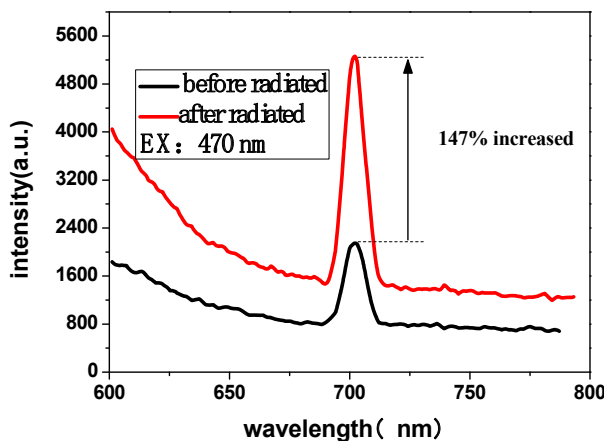

Fig. 9. Emission spectra of epoxy resin / $Mn_3B_7O_{13}Cl$ composite coating before and after irradiation

solution of $Mn_3B_7O_{13}Cl$ containing Pca21 space basis was obtained by the intrinsic phase method of APEX3 program, and the final refinement was completed by the SHELXL program package [66-68]. The pyroelectric coefficient is obtained by measuring the current in the TF-3000 ferroelectric system [69-71]. In the infrared spectrum, the bending vibration of (BO_3) and (BO_4) is in the range of 400-700 cm^{-1}, the symmetric vibration of (BO_3) and (BO_4) is in the range of 700-850 cm^{-1} and 850-950 cm^{-1}, (BO_3) and (BO_4) symmetry vibration is in 950-1100 cm (1300-1500 cm^{-1}) and 1100-1300 cm^{-1} within the scope of the peak on behalf of Mn-Cl octahedron bending vibration [72-75]. The melting point of $Mn_3B_7O_{13}Cl$ is 1360 K and the quadrature cubic phase transition temperature is 698 K, representing the polar center symmetric phase transition [76]. $Mn_3B_7O_{13}Cl$ is also a piezoelectric or thermoelectric or ferroelectric and magnetically ordered material [77]. The pyroelectric measurement of z-cut crystals was carried out by the current method [78]. $Mn_3B_7O_{13}Cl$ has a high Curie temperature and the thermoelectric coefficient is almost unchanged in the range of 300 K and 400 K, which is very similar to the properties of lead titanate [79]. In the temperature range of 300~400 K, the relative dielectric constant of [001] crystal direction of $Mn_3B_7O_{13}Cl$ is about 11.5, which is high in all polar minerals, especially borate minerals [80]. Figures of merit (FOMs) are calculated based on the current response and high voltage response of the infrared detection device [82,83]. The overall phase diagram of thermoelectric properties consisting of organic and inorganic materials is divided into two distinct regions. For organic pyroelectric materials represented by TGS and PVDF [84-86], although the amount of F_V is extremely high, low T_C limits the application scenarios of these materials. Meanwhile, in inorganic pyroelectric materials, $BaTiO_3$ has a lower T_C and F_V [87], while PZT, $PbTiO_3$ and $PbZrO_3$ derived materials contain toxic Pb element [88,89]. $LiTaO_3$, as one of the few commercially available pyroelectric materials, has high T_C and F_V [90].

With the development of electronic equipment, radar and aircraft stealth technology, electromagnetic shielding and absorbing materials are attracting more and more attention. Borate compounds have been widely used as dielectric materials and nuclear protection materials due to their rich structural types and excellent properties [17-18], attracting much attention from scholars.

However, compounds with unique macromolecular structures such as $Mn_3B_7O_{13}Cl$, which are rare, have not been studied much. Liang et al. [19] synthesized nano-sized $Mn_3B_7O_{13}Cl$ in a sol-gel system using $MnCl_2$ and $Na_2B_4O_7$ as precursors. The synthesis of nano-$Mn_3B_7O_{13}Cl$ powders was compacted and sintered using spark plasma sintering (SPS), and the dielectric properties of $Mn_3B_7O_{13}Cl$ were tested at a low frequency (0~1 MHz) and the electromagnetic properties of $Mn_3B_7O_{13}Cl$ at a high frequency (1~18 GHz), respectively, as given in Fig. 10. Fig. 10(a) shows that the dielectric constant of nano-$Mn_3B_7O_{13}Cl$ decreases rapidly with the increase of frequency before 200 k Hz, from 8.2 F / m to 4.5 F / m. After 200 k Hz, the dielectric constant changes little. Compared with the synthetic nano-$Mn_3B_7O_{13}Cl$, the dielectric constant of raw $Mn_3B_7O_{13}Cl$ varies smoothly with the electromagnetic frequency, and the dielectric constant is between 6.8 and 7.0 after 400 KHz. Fig. 10(b) shows that with the increase of frequency, the loss of nano-$Mn_3B_7O_{13}Cl$ decreases gradually, and its change rule is like that of dielectric constant. The loss decreases significantly before 200 kHz, and decreases from 0.3 to 0.14 after 200 kHz to 1 MHz. The results show that nano-$Mn_3B_7O_{13}Cl$ has good electromagnetic properties, small dielectric constant, and moderate loss. It can be used in microwave dielectric ceramic substrate materials, and may be used in microwave attenuation materials and wave absorbing materials.

5. Antitumor and antibacterial properties of $Mn_3B_7O_{13}Cl$

In the past studies, the use of boron-containing compounds as antitumor drugs [91,92] and their bactericidal effects [93,94] have been extensively reported, among which boric acid has been widely used in the field of antiviral antibacterial [95,96]. The author and his research team conducted a field investigation in the chambersite ore cave in Tianjin, China, and found that there was no odor or mosquito flies in an abandoned chambersite ore cave for many years, and the water in the cave was very clear. A village downstream of the $Mn_3B_7O_{13}Cl$ deposit is known locally as "Longevity Village". Therefore, $Mn_3B_7O_{13}Cl$ may have antitumor and antibacterial effects. $Mn_3B_7O_{13}Cl$'s inhibitory ef-
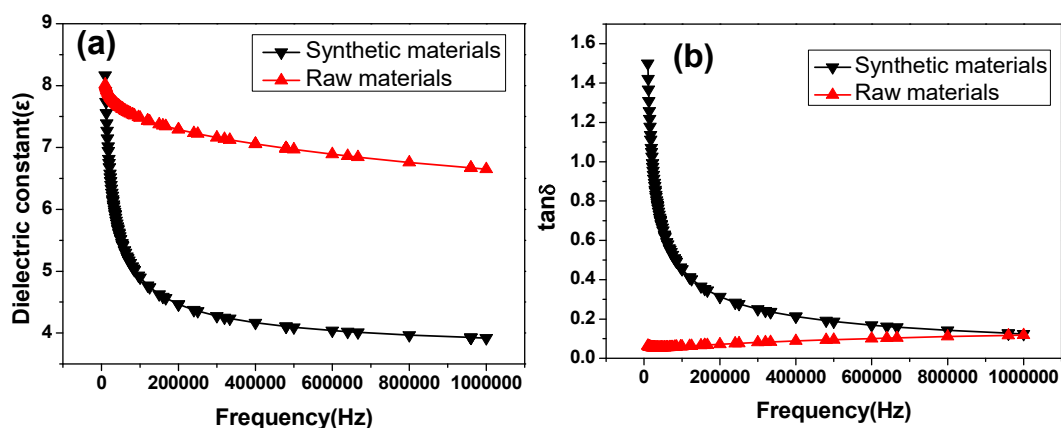
Fig. 10. Permittivity (a) and loss (tanδ) (b) of synthetic $Mn_3B_7O_{13}Cl$ and raw $Mn_3B_7O_{13}Cl$

fect on the human lung cancer cell A549 was examined by Liang et al. [97]. Fig. 11 displays the inhibitory rate of raw $Mn_3B_7O_{13}Cl$ (b) and manufactured nano-$Mn_3B_7O_{13}Cl$ (a) on the lung cancer cell A549. The outcomes demonstrated that as the experimental duration was extended, the inhibition rates of the two samples at various doses on tumor cells increased. The inhibition rates were not high, both were less than 50% within 24 h after the medication interacted with the tumor cells. The inhibition rates of the synthetic and raw $Mn_3B_7O_{13}Cl$, however, reached more than 70% when the reaction time approached 48 h. With a 75% inhibition rate, the ideal concentration of nano-$Mn_3B_7O_{13}Cl$ for A549 was 150 g/ml. On A544, 100 g/ml of raw $Mn_3B_7O_{13}Cl$ provided the best results, with an 80% inhibition rate. The anti-tumor impact of the raw $Mn_3B_7O_{13}Cl$ was better. Comparing this inhibition rate to that of various anticancer medications, it is noticeably better [98].
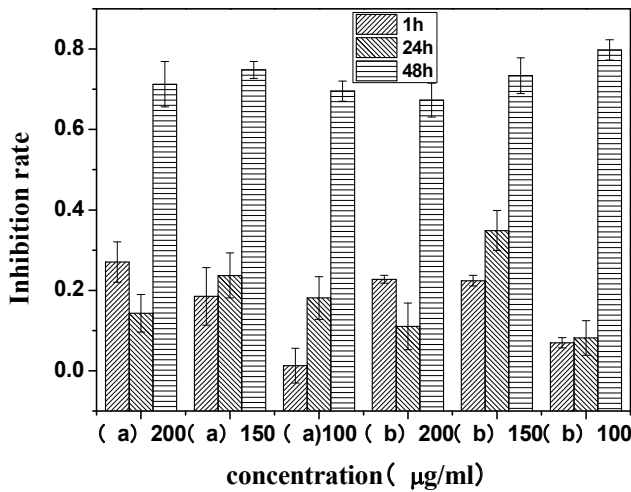

Fig. 11. Inhibition rates of synthetic $Mn_3B_7O_{13}Cl$ (a) and raw $Mn_3B_7O_{13}Cl$ (b) to lung cancer A549

The inhibitory effect (OD value) of $Mn_3B_7O_{13}Cl$ on Escherichia coli BL21 is shown in Fig. 12. The calculations indicated that the concentration of bacteria in the solution con-

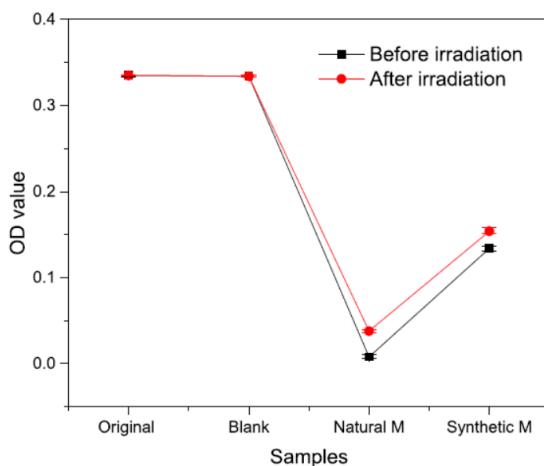Fig. 12. Sterilization OD value of bacterium samples with synthetic and raw $Mn_3B_7O_{13}Cl$ (M) added under gamma radiation

taining nano- $Mn_3B_7O_{13}Cl$ (Synthetic M) fell by 97.6%, and the findings demonstrated a considerable reduction in the concentration of bacteria in the solution containing raw $Mn_3B_7O_{13}Cl$ (Natural M) [99-102]. However, the concentration of synthetic nano-$Mn_3B_7O_{13}Cl$ also decreased, though it did so with a much lesser fall range than that of raw $Mn_3B_7O_{13}Cl$, which fell by 60%. The bacterial concentration remained essentially unchanged in the control group. As a result, $Mn_3B_7O_{13}Cl$ kills Escherichia coli BL21, with raw $Mn_3B_7O_{13}Cl$ being the most effective, which is consistent with the findings of the antitumor experiment.

6. Tribological and wear properties of $Mn_3B_7O_{13}Cl$

The average size of the prepared Mn3B7O13Cl nanoparticles is about 30 nm by sol-gel method. Mn3B7O13Cl nanoparticle is an excellent friction-reducing and antiwear lubricant [103-105]. The common nano-Cu, nano-Fe nanoparticles, and commercial oil are used as a reference experiment. Loadcarrying capacity of nano-Mn3B7O13Cl added oil is stronger than those of base oil, nano-Cu, and nano-Fe added oil with the same content; it reaches the value of 637 N and the WSD is 0.52 mm when the concentration is only 0.2 wt.% and given in Fig. 13. Meanwhile, $Mn_3B_7O_{13}Cl$ nanoparticles as an efficient antiwear lubricant and commercial oil were measured in the sliding wear between tantalum strip and 52100 bearing steel ball by MFT-3000 friction and wear tester at an optimized additive concentration (0.2 wt.%). Coefficient of friction of tantalum strips is reduced by 41.5% compared with that of the commercial oil. Furthermore, the antiwear and friction-reducing behavior of nano-$Mn_3B_7O_{13}Cl$ is attributed to boron element by XPS studies, which revealed that the remarkable lubrication performances of nano-$Mn_3B_7O_{13}Cl$ is usually ascribed to a protective tribofilm (~30 nm) on the tantalum strip surface, the adsorbed boron layers, and tribosintered nano-$Mn_3B_7O_{13}Cl$, constituting the tribofilm during the friction contact process, given in Fig. 14. Therefore, $Mn_3B_7O_{13}Cl$ nanoparticle is an efficient antiwear lubricant in the sliding wear between tantalum and steel ball, protecting interacting surfaces to avoid the severe wear.

Copper-based powder metallurgy friction materials is one of the most widely used friction materials. In order to further improve the performance of copper-based friction materials, researchers choose to add a second phase particle to the copper base as the reinforcement phase [106,107]. Manganese and copper are used because they are infinitely miscible. Boron is also a commonly used element in wear-resistant materials. Because the structure of $Mn_3B_7O_{13}Cl$ contains a lot of manganese and boron elements, the addition of $Mn_3B_7O_{13}Cl$ is helpful to improve the tribological properties of copper-based friction sheet. Gong et al. [108] and Shu et al. [109] added raw $Mn_3B_7O_{13}Cl$ powder with mass fraction of 0.5% to the copper-base powder, and made copper-based friction sheet samples by high-energy ball milling combined with discharge plasma sintering. The effects of $Mn_3B_7O_{13}Cl$ with different particle sizes on the friction coefficient of copper-based friction materials were studied, and
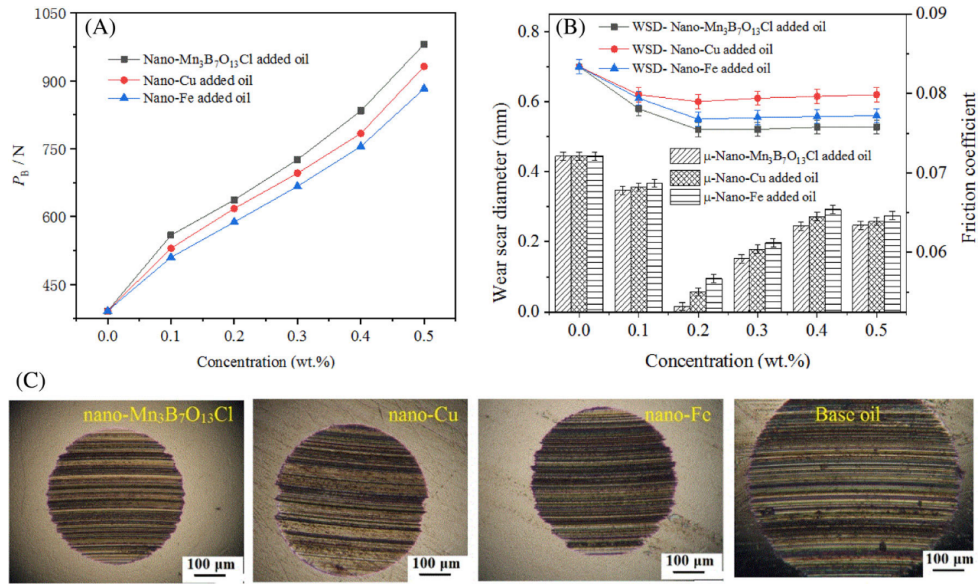
Fig. 13. P_B value (A), the wear scar diameter and coefficient of friction (B) as a function of concentration of the additives, and the wear surface morphology of balls (0.2 wt.%) (C)
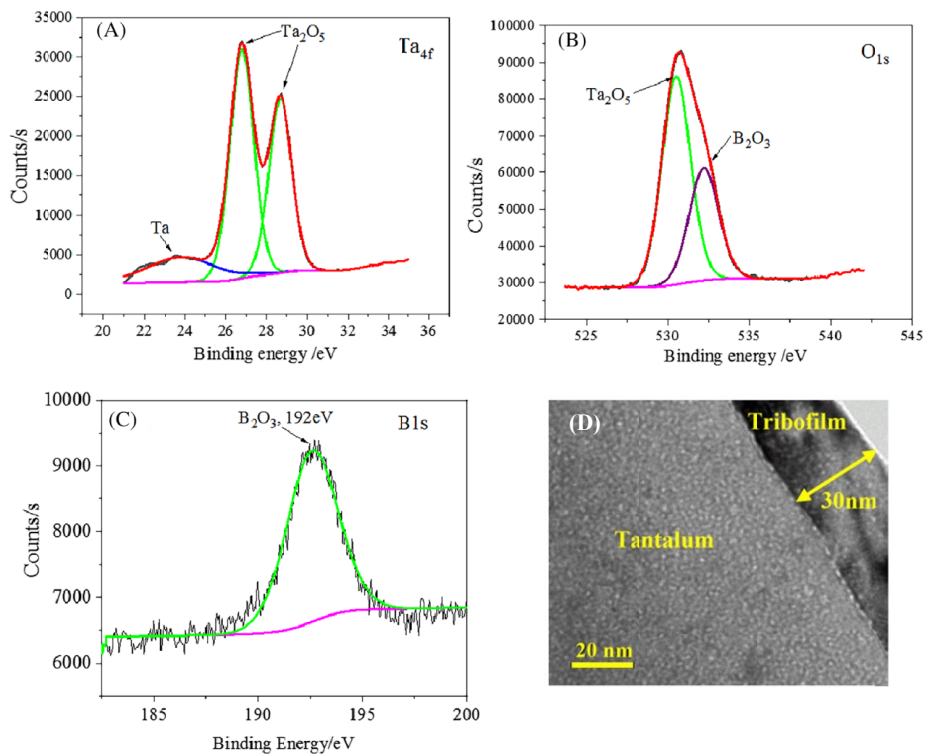

Fig. 14. X-ray photoelectron spectroscopy of the surface of tantalum. (A) Ta_{4f} region, (B) O_{1s} region, (C) B_{1s} region, and (D) Focused ion beam-transmission electron microscopy of tribofilm formed on the surface of tantalum with nano-$Mn_3B_7O_{13}Cl$ after sliding

the results are shown in Fig. 15. The results show that the friction coefficient of copper-based powder is increased obviously after adding a very small amount of $Mn_3B_7O_{13}Cl$. The friction coefficient of Cu base material ($0^{\#}$) without adding $Mn_3B_7O_{13}Cl$ is 0.171, and that of adding $Mn_3B_7O_{13}Cl$ is 0.187~0.211. In addition, the author also studied the effects of adding different particle sizes of $Mn_3B_7O_{13}Cl$ on the wear rate and hardness, and the results are shown in Fig. 16. The results show that the wear rate of Cu-based material without $Mn_3B_7O_{13}Cl$ is 2.01×10^{-14} $m^3 \cdot J^{-1}$,

and the wear rate of Cu-based material with $Mn_3B_7O_{13}Cl$ decreases with the decrease of particle size, while the hardness curve shows an opposite trend. The results show that adding $Mn_3B_7O_{13}Cl$ to copper can improve the friction coefficient and reduce the wear rate.

In addition, the study of the relationship of the microstructure and properties has been reported in the previous work [110-112], which provides a theoretical basis for further development and application of $Mn_3B_7O_{13}Cl$.
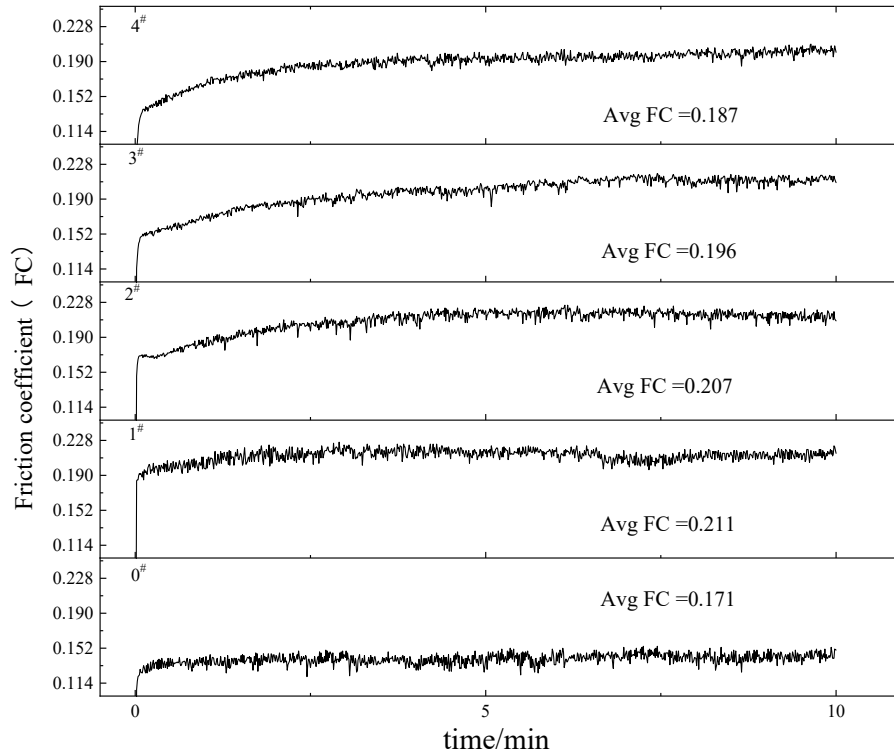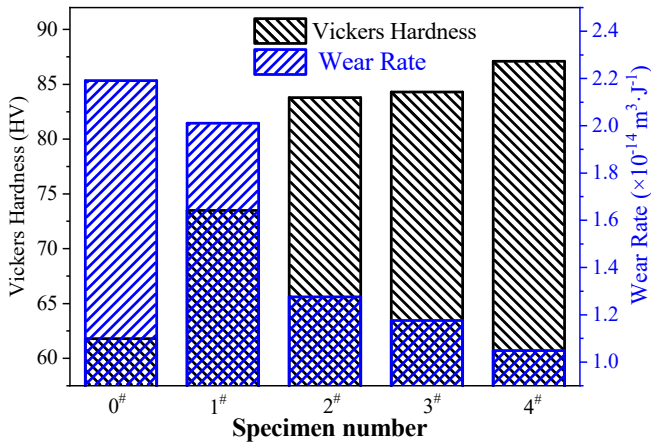
Fig. 15. Friction coefficients of samples

Fig. 16. Wear rate and microhardness of samples

9. Summary and prospective

Chambersite is a rare mineral, only in the world China unique chambersite deposit, it is the precious wealth left to us by nature. The molecular formula of chambersite is $Mn_3B_7O_{13}Cl$, and it has a boron-oxygen skeleton rhombic crystal structure. Nano-$Mn_3B_7O_{13}Cl$ was successfully synthesized by the improved sol-gel method, and its crystal structure was consistent with that of raw $Mn_3B_7O_{13}Cl$. The crystal structure was calculated and simulated by EMS software. The structure of $Mn_3B_7O_{13}Cl$ is similar to that of spinel. There are many tetrahedral and octahedral sites in the crystal, and Mn^{2+} occupies these two sites, emitting green light (500 nm-540 nm) and red light (670 nm-730 nm) under the excitation of blue light (450 nm-490 nm).

When the excitation wavelength is increased, the emission spectrum of manganite is red shifted, which is mainly due to the different crystal field strength caused by the existence of aggregates of different sizes in manganite particles. The luminescence property of $Mn_3B_7O_{13}Cl$ has the property of transforming "cool light" into "warm light", which can be applied to make energy conversion glass and has good thermal insulation effect. It also has good photoluminescence, electromagnetic properties, anti-tumor, anti-bacterial properties, gamma ray irradiation and neutron irradiation properties and tribological properties. At the same time, it also has relatively stable electromagnetic properties in the low frequency electromagnetic wave and microwave frequency band, and can be applied in the field of electromagnetic shielding materials by introducing appropriate absorbers. Copper-base P/M friction material is a key material in brakes for high speed and heavy load equipment, and plays an important role in aerospace and automobile manufacturing industry in our country. The same components as the copper-base friction plate material currently used in our country's automobile, and introduces $Mn_3B_7O_{13}Cl$ into the friction material, the friction coefficient of the friction plate is more stable, and the wear rate is reduced. Thus, the friction and wear performance of the copper-based friction plate is improved. The introduction of $Mn_3B_7O_{13}Cl$ is of great significance for the service life and safety of copper-based friction materials. However, there are few reports on its theoretical research and practical application at home and abroad, so more in-depth research is needed to discover its new physical and chemical properties and provide theoretical basis for further development and application of $Mn_3B_7O_{13}Cl$ in the word.

68

REFERENCES

[1] Y. Sun, Z. Li, M.H. Lee, Z. Yang, S. Pan, B. Sadeh, J. Phys. Soc. Jpn. **86** (4), 044401 (2017).

[2] Z. Wang, H. Qiao, R. Su, B. Hu, X. Yang, C. He, X. Long, Adv. Funct. Mater. **28** (41), 1804089 (2018).

[3] Z. Xiong, J. He, B. Hu, P. Shan, Z. Wang, R. Su, C. He, X. Yang, X. Long, ACS Appl. Mater. Interfaces. **12** (38), 42942-42948 (2020).

[4] В.Ф. Велов, Study on the chambersite $Mn_3B_7O_{13}Cl$ with nucleon γ ray resonance absorption. J. M. Geol Geochem, Wiley (1980).

[5] C.D. Xiao, J. Zhang, B.H. Zhang, J.L. Liu, Z.Y Qin, S.W. Li, Geol. Survey Res. **30** (3), 186-195 (2007).

[6] J. Guo, R. Sun, F. Chen, M.N. Hao, Y.X. Ma, Y.T. Wu, D.X. Hu, Z.Y. Zhang, T.M. Liu, D.Z. Meng, C.C Zhao, J. Crystal Growth. **581**, 126510 (2022).

[7] Y.S. Zeng, Acta Geol. Sin. **57** (4), 401-410 (1983).

[8] S. Xiong, D. Liang, L. Cao, J.L. Sun, Mater. Lett. **178**, 87-96 (2016).

[9] A. Tomita, T. Sato, K. Tanaka, Y. Kawabe, M. Shirai, K. Tanaka, E. Hanamura, J. Lumin. **109** (1), 19-25 (2004).

[10] N. Taghavinia, H. Makino, T. Yao, Appl. Phys. Lett. **83** (22), 4616 (2003).

[11] D.X. Jiang, L.X. Cao, G. Su, H. Qu, D. Sun, Appl. Surf. Sci. **253** (24), 9330 (2007)

[12] A. García J., A. Remón, J. Piqueras, J. Appl. Phys. **62** (7), 3058 (1987).

[13] W.R. Gao, X.M. Wang, W.Q. Xu, Mater. Sci. Eng. C. **42**, 333-342 (2014).

[14] J.P. Yuan, W.W. Guo, E.K. Wang, Anal. Chim. Acta. **706** (2), 338-342 (2011).

[15] Y. Tian, Y.Y. Cao, F. Pang,G.Q. Cheng, X. Zhang, Rsc. Adv. **4** (81), 43204 (2014).

[16] S. Dhanya, V. Saumya, T.P. Rao, Electrochim Acta **102**, 299-305 (2013).

[17] J.L. Luce, K.I. Schaffers, D.A. Keszler, Inorg. Chem. **33** (11), 2453 (1994).

[18] Z.T. Yu, PhD thesis, Borates and Uranyl Compounds with Optical and Photoelectrical Functions:Synthesis, Structures and Properties. Jilin University, Changchun, China (2004).

[19] D. Liang, PhD thesis, Study on the Structure, haracteristic, and application of chambersite and tungsten-based nanomaterial. University of Science and Technology Beijing, China (2015).

[20] A. El-Sayed Abdo, M.A. El-Sarraf, F.A. Gaber, Annals of Nuclear Energy **30** (2), 175-187 (2003).

[21] M. Kamoshida, M. Oda, T. Nishi T, High temperature resistant polymer; hardening epoxy resin. Google Patents, (2004).

[22] M. Atsuhiko, S. Shinji, O. Koichi, S. Satoshi, V. Yury, K. Atsushi, N. Takeo, T. Hiroshi, K. Yusuke, Y. Shigeru, M. Makoto, Journal of Nuclear Materials **367**, 1085-1089 (2007).

[23] S. Kaur, K.J. Singh, Anals. Nuclear Energy. **63**, 350-354 (2014).

[24] M. Dong, S. Zhou, X. Xue, M.I. Sayyed, D. Tishkevich, A. Trukhanov, C. Wang, Progress in Nuclear Energy **146**, 104155 (2022).

[25] A.G. Castellanos-Guzman, V.M. Soto García, L. Bayarjargal, E. Haussühl, B. Winkler, Ferroelectrics **498** (1), 36-39 (2016).

[26] W. Schnelle, E. Gmelin, O.C. Schmid, Journal of Thermal Analysis and Calorimetry **56**, 365-370 (1999).

[27] M. Dong, X. Xue, A. Kumar, H. Yang, M.I. Sayyed, S. Liu, E. Bu, J. Hazard Mater. **344**, 602-614 (2018).

[28] M. Dong, X. Xue, Z. Li, H. Yang, M.I. Sayyed, B.O. Elbashir, Prog. Nucl. Energy **106**, 140-145 (2018).

[29] M.G. Dong, X.X. Xue, Y. Elmahroug, M.I. Sayyed, M.H.M. Zaid, Results Phys. **13**, 102129 (2019).

[30] M. Dong, S. Zhou, X. Xue, X. Feng, M.I. Sayyed, M.U. Khandaker, D.A. Bradley, Radiat. Phys. Chem. **188**, 109601 (2021).

[31] D. Fan, P. Yang, R. Wang, Ore Geol. Rev. **15** (1-3), 15-29 (1999).

[32] D.K. Gaikwad, S.S. Obaid, M.I. Sayyed, R.R. Bhosale, V.V. Awasarmol, A. Kumar, M.D. Shirsat, P.P. Pawar, Mater. Chem. Phys. **213**, 508-517 (2018).

[33] G. Goldstein, J. Inorg. Nucl. Chem. **28** (4), 937-939 (1966).

[34] L.L. Gong, L. Cao, C.C. Jia, D. Liang, J. University of Science and Technology Beijing **36**, 354-358 (2014).

[35] Y. Harima, Y. Sakamoto, S. Tanaka, M. Kawai, Nucl. Sci. Eng. **94** (1), 24-35 (1986).

[36] R.E. Honea, F.R. Beck, J. Earth Planet. Mater. **47** (5-6), 665-671 (1962).

[37] L. Huo, J.L. Liu, Y.H. Ma, Radiation Dose and Protection. Interaction of ionizing radiation with matter,Publishing House of Electronic Industry, Beijing (2015).

[38] R. Karimzadeh, S. Stummer, T. Böck, H., Nucl. Eng. Des. **241** (8), 2859-2864 (1989).

[39] B. Krusche, K.P. Lieb, H. Daniel, T. Von Egidy, G. Barreau, H.G. B¨orner, R. Brissot, C. Hofmeyr, R. Rascher, Nucl. Phys. **386** (2), 245-268 (1982).

[40] G. Lakshminarayana, Y. Elmahroug, A. Kumar, M.G. Dong, D.E. Lee, J. Yoon, T. Park, Ceram. Int. **46** (10), 16620-16635 (2020).

[41] D. Liang, S. Xiong, Radiat. Eff. Defect Solid **174** (7-8), 596-605(2019).

[106] D. Liang, L. Cao, C.C. Jia, Powder Metallurgy Technology **33**, 111-115 (2015).

[42] S.H. Miri Hakimabad, Asian J. Exp. Sci. **21**, 249-258 (2007).

[43] U. Perişanoğlu, H.O. Tekin, A.S. Abouhaswa, E. Kavaz, Radiat. Phys. Chem. **179**, 109262 (2021).

[44] J. Ranft, Nucl. Instrum. Methods **48** (1), 133-140 (1967).

[45] B. Ahmed, G.B. Shah, A.H. Malik, M. Rizwan, Appl. Radiat. Isot. **155**, 108901 (2022).

[46] D. Liang, L. Cao, C. Jia, Powder Metallurgy Technology **33**, 111-115 (2015).

[47] K. Aizu, Phys. Rev. **136** (3A), A753-A758 (1964).

[48] W. Zhang, R.G. Xiong, Chem. Rev. **112** (2), 1163-1195 (2012).

[49] K.F. Wang, J.M. Liu, Z.F. Ren, Adv. Phys. **58** (4), 321-448 (2009).

[50] V. Kocsis, T. Nakajima, M. Matsuda, A. Kikkawa, Y. Kaneko, J. Takashima, K. Kakurai, T. Arima, F. Kagawa, Y. Tokunaga, Y. Tokura, Y. Taguchi, Nat. Commun. **10**, 1247 (2019).

[51] X. Fang, D. Wei, D. Liu, W. Zhong, R. Ni, Z. Chen, X. Hu, Y. Zhang, S.N. Zhu, M. Xiao, Appl. Phys. Lett. **107** (16), 161102 (2015).

[52] R.J. Nelmes, J. Phys., C: Solid State Phys. **7** (21), 3840–3854 (1974).

[53] R.M. Honea, F.R. Beck, Mineral. **47**, 665-671 (1962).

[54] H. Schmid, J. Phys. Chem. Solids. **26** (6), 973-976 (1965).

[55] F. Kubel, O. Zeitschrift für Kristallographie – Crystalline Mater. **211**, 924 (1996).

[56] R.G.P. Mcquaid, M.P. Campbell, R.W. Whatmore, A. Kumar, J.M. Gregg, Nat. Commun. **8**, 15105 (2017).

[57] H. Schmid, W. Schnelle, Phys. Rev. B. **91**, 184411 (2015).

[58] A. Li, L. Xu, S. Li, Y. He, R. Zhang, Y. Zhai, Nano Res. **8** (2) 554-565 (2015).

[59] H. Huang, L. Liu, S. Jin, W. Yao, Y. Zhang, C. Chen, J. Am. Chem. Soc. **135** (49), 18319-18322 (2013).

[60] Y. Sun, Z. Li, M.-H. Lee, Z. Yang, S. Pan, B. Sadeh, J. Phys. Soc. Jpn. **86** (4), 044401 (2017).

[61] Z. Wang, H. Qiao, R. Su, B. Hu, X. Yang, C. He, X. Long, Adv. Funct. Mater. **28** (41), 1804089 (2018).

[62] Z. Xiong, J. He, B. Hu, P. Shan, Z. Wang, R. Su, C. He, X. Yang, X. Long, ACS Appl. Mater. Interfaces. **12** (38), 42942-42948 (2020).

[63] H. Schmidt, H. Tippmann, Ferroelectrics **20** (1), 21-36 (1978).

[64] K. Nassau, J.W. Shiever, J. Cryst. Growth. **16** (1), 59-61 (1972).

[65] A.G. Castellanos-Guzman, J. Campa-Molina, J. Reyes-Gomez, J. Microsc. **185**, 1-8 (1997).

[66] G.M. Sheldrick, T.R. Schneider, Methods Enzymol. **277**, 319-343 (1997).

[67] O.V. Dolomanov, L.J. Bourhis, R.J. Gildea, J.A.K. Howard, H. Puschmann, Sect. A: Found. Adv. **65**, s313 (2009).

[68] G.J. Zhou, H. Liu, K.R. Chen, X.H. Gai, C.C. Zhao, L.B. Liao, K. Shen, Z.J. Fan, Y. Shan, J. Alloys Compd. **744**, 328-336 (2018).

[69] K. Chen, X. Gai, G. Zhou, Y. Shan, C. Zhao, K. Shen, Z. Fan, Ceram. Int. **45** (8), 10684-10690 (2019).

[70] I.A. Chernyshova, O.S. Vereshchagin, O.V. Malyshkina, A.G. Goncharov, I. A. Kasatkin, M.N. Murashko, A.A. Zolotarev, O.V. Frank-Kamenetskaya, J. Solid State Chem. **303**, 122512 (2021).

[71] J. Ju, H.M. Li, Y.X. Wang, J.H. Lin, C. Dong, J. Mater. Chem. **12**, 1771-1774 (2002).

[72] R.L. Frost, A. Lopez, R. Scholz, Y.F. Xi, Spectrochim. Acta Part A, Mol. Biomol. Spectrosc. **120**, 270-273 (2013).

[73] T. Ibroska, A.S. Kipcak, Y.S. Aydin, E. Derun, S. Piskin, Turk. J. Chem. **39**, 1025-1037 (2015).

[74] R. Zhang, H. Xu, M.M. Li, Rock Miner. Anal. **37**, 139-145 (2018).

[75] O. Crottaz, P. Schobinger-Papamantellos, E. Suard, C. Ritter, S. Gentil, J.-P. Rivera, H. Schmid, Ferroelectrics **204** (1), 45-55 (1997).

[76] S. Jachalke, E. Mehner, H. Stöcker, J. Hanzig, M. Sonntag, T. Weigel, T. Leisegang, D.C. Meyer, Appl. Phys. Rev. **4** (2), 021303 (2017).

[77] J.P. Remeika, A.M. Glass, Mater. Res. Bull. **5** (1), 37-45(1970).

[78] A.G. Castellanos-Guzmån, J.C. Burfoot, H. Schmid, P. Tissot, Ferroelectrics **36** (1), 411-414 (1981).

[75] C. Rai, K. Sreenivas, S.M. Dharmaprakash, J. Cryst. Growth. **312** (2), 273-275 (2010).

[76] W.R. Li, G. Tang, G.Z. Zhang, H.M. Jafri, J. Zhou, D. Liu, Y. Liu, J.S. Wang, K.J. Jin, Y.M. Hu, H.S. Gu, Z. Wang, J.W. Hong, H.B. Huang, L.Q. Chen, S.L. Jiang, Q. Wang, Sci. Adv. **7**, eabe3068 (2021).

[77] S.B. Lang, Phys. Today. **58** (8), 31-36 (2005).

[78] S. Bauer, S.B. Lang, IEEE T. Dielect. El. In. **3**, 647-676 (1996).

[79] A. Saxena, M. Fahim, V. Gupta, K. Sreenivas, J. Phys. D: Appl. Phys. **36** (24), 3168-3175 (2003).

[80] M. Aggarwal, M. Kumar, R. Syal, V.P. Singh, A.K. Singh, S. Dhiman, S. Kumar, J. Mater. Sci.: Mater. Electron. **31** (3), 2337-2346 (2020).

[81] Y. Zhang, M. Xie, J. Roscow, Y. Bao, K. Zhou, D. Zhang, C.R. Bowen, J. Mater. Chem. A. **5** (14), 6569-6580 (2017).

[82] H. He, X. Lu, E. Hanc, C. Chen, H. Zhang, L.i. Lu, J. Mater. Chem. C. **8** (5), 1494-1516 (2020).

[83] F. Tang, S. Long, X. Yang, M. Yang, J. Quan, S. Lin, D. Ma, Y. Zhu, B. Wang, J. Phys. D: Appl. Phys. **51** (39), 395101 (2018).

[82] B. Alshahrani, I.O. Olarinoye, C, Mutuwong, C. Sriwunkum, H.A. Yakout, H.O. Tekin, M.S. Radiat. Phys. Chem. **183**, 109386 (2021).

[83] I.I. Bashter, Ann. Nucl. Energy. **24** (17), 1389-1401 (1997).

[84] M.J. Berger, J.H. Hubbell, NBSIR 87-3597, XCOM: Photon Cross Sections on a Personal Computer. National Institute of Standards and Technology, Gaithersburg, MD 20889, USA (1987).

[85] D.A. Brown, M.B. Chadwick, R. Capote, A.C. Kahler, A. Trkov, M.W. Herman, A.A. Sonzogni, Y. Danon, A.D. Carlson, M. Dunn, D.L. Smith, Nucl. Data Sheets. **148**, 1-142 (2018).

[86] N.I. Cherkashina, V.I. Pavlenko, A.V. Noskov, Radiat. Phys. Chem. **159**, 111-117 (2019).

[87] D.L. Chichester, B.W. Blackburn, Mater. Atoms, **261** (1-2), 845-849 (2007).

[88] A.B. Chilten, J.K. Shultis, R.E. Faw, Principle of Radiation Shielding. Prentice-Hall, Englewood Cliffs, N.J. (1984).

[89] C. Coceva, A. Brusegan, C. Van der Vorst, Nucl. Instrum. Methods Phys. Res. Sect. A Accel. Spectrom. Detect. Assoc. Equip. **378** (3), 511-514 (1996).

[90] M.G. Dong, X.X. Xue, V.P. Singh, H. Yang, Z.F. Li, M.I. Sayyed, Nucl. Sci. Tech. **29** (4), 1-8 (2018).

[91] K. Lin, G. Zhang, N. Fu. Organic Chemistry. **24** (03), 228-232 (1985).

[92] G. Zhang, G. Yuan. Organic Chemistry **21** (06), 409-412 (1982).

[93] M. Feld, V. Shpacovitch, C. Ehrhardt, M. Fastrich, T. Goerge, S. Ludwig, M. Steinhoff, BioMed Research International **13**, 2013 (879080).

70

[94] Y. Wang, X. Wang, L. Occhiena, Y.D. Zhou, D. Chuang, A. Sun, D.L. Gill, Biophysical Journal **106** (2), 315a (2014).

[95] S.M. Sammeta, L. Wang, S.K. Mutyam, O.L .Kathleen, C.E. Green, M.H. Werner, T. Kelly, G.N. Shankar, Pharmaceutical Development and Technology **20** (2), 167-175 (2013).

[96] L. Moni, L. Banfi, A.L. Basso, L. Carcone, M. Rasparini, R. Riva, The Journal of Organic Chemistry **80** (7), 502829 (2015).

[97] C.M. Hull, M.J. Levin, S.K. Tyring, S.L. Spruance, Antimicrobial Agents and Chemotherapy **58** (3), 1273-1278 (2014).

[98] Y.J. Wang, PhD thesis, Inhibition and mechanism of Pingfei Compound on the proliferation of human lung adenocarcinoma A549 cells, Beijing University of Chinese Medicine, Beijing, China (2014).

[99] Z. Hao, Acta Geologica Sinica: English Edition. **89** (5), 1762-1763 (2015).

[100] H.N. Bai, Z. Ji, L. Cao, T. Qin, C.C. Jia, S.C. Hao, Fenmo Yejin Jishu/Powder Metallurgy Technology **36** (1), 73-78 (2018) (In Chinese).

[101] K. Heid, G. Nolze, G. Völksch, H. Gerhard, Zeitschrift für Kristallographie – Crystalline Materials **228** (9), 467-475 (2013).

[102] F. Kubel, O. Crottaz, **211** (12), 924-925 (1996).

[103] E. Şakar, Ö.F. Özpolat, B. Alım, M.I. Sayyed, M. Kurudirek, Radiat. Phys. Chem. **166**, 108496 (2020).

[104] H.J. Park, H. Kang, H.C. Lee, .Y. Cho, Ann. Nucl. Energy **131**, 443-459 (2019).

[105] S. Xiong, D. Liang, H. Wu, B. Zhang, Lubric. Sci. **32** (3), 121-130 (2020).

[106] F.T. Wang, Y.C. Wu, W.F. Wang, J.H. Zhang, Nonferrous Met. **59** (1), 38-43 (2007).

[107] Y. Zhang, Y.C. Zhou, Acta Metall. Sin. **36** (6), 662 (2000).

[108] L.L. Gong, L. Cao, C.C. Jia, L. Cao, X.N. Shu, Powder Metall. Technol. **31** (4), 279 (2013).

[109] X.N. Shu, L. Cao, C.C. Jia, D. Liang, L.L. Gong, Mater. Sci. Eng. Powder Metall. **220** (2), 187 (2015).

[110] Q. Wang, H. Xu, S. Gao, L.Yang, Earth Science Frontiers **20** (3), 123-130 (2013).

[111] S. Xiong, X. Zhang. Powder Metall. Met. Ceram. **61**, 424-431 (2022).